Environmental Science Nano

Engineered zinc oxide-based nanotherapeutics boost systemic antibacterial efficacy against phloem-restricted diseases

Journal:	*Environmental Science: Nano*
Manuscript ID	EN-ART-03-2022-000263.R1
Article Type:	Paper

Engineered zinc oxide-based nanotherapeutics boost systemic antibacterial efficacy against phloem-restricted diseases

Mikhael Soliman[1,2,°], Briana Lee[1,°], Ali Ozcan[1,3,‡, δ], Takat B. Rawal[4,5, #,δ], Mikaeel Young[1,6], Hajeewaka C. Mendis[1,7], Parthiban Rajasekaran[1], Torus Washington II[1], Sai Venkatesh Pingali[8], Hugh O'Neill[5,8], Andre Gesquiere[1,3], Leonardo De La Fuente[7], Loukas Petridis[4,5], Evan Johnson[9], James Graham[9], Swadeshmukul Santra[1,2,3,6]*, Laurene Tetard[1,10]*

[1] NanoScience Technology Center, University of Central Florida, Orlando, FL, 32826, USA
[2] Material Science Engineering Department, University of Central Florida, Orlando, FL, 32816, USA
[3] Department of Chemistry, University of Central Florida, Orlando, FL 32816, USA
[4] UT/ORNL Center for Molecular Biophysics, Oak Ridge National Laboratory, Oak Ridge, TN, 37830
[5] Department of Biochemistry and Cellular and Molecular Biology, University of Tennessee, Knoxville,
[6] Burnett School of Biomedical Sciences, University of Central Florida, Orlando, FL 32816, USA
[7] Department of Entomology and Plant Pathology, Auburn University, Auburn, AL 36849
TN, 37996
[8] Neutron Scattering Division, Oak Ridge National Laboratory, Oak Ridge, TN, 37830
[9] Citrus Research and Education Center, University of Florida, Lake Alfred, Florida 33850, USA
[10] Department of Physics, University of Central Florida, Orlando, FL 32816, USA
[°] Equal contributions
[δ] Equal contributions
[‡] Current institution: Vocational School of Technical Sciences, Karamanoglu Mehmetbey University, Karaman, 70200, Turkey
[#] Present address: Department of Physics, University of Houston, Houston, TX, 77204

*Corresponding authors: swadeshmukul.santra@ucf.edu; laurene.tetard@ucf.edu

Environmental Significance Statement

Vascular diseases in plants are becoming a widespread threat to food crop production and sustainability. Nanoengineered particles have shown some promise as new alternatives to conventional antibiotics but systemic delivery of the functional material to tackle pathogens lodged in the phloem or xylem remains challenging. The ability to study the behavior of antibacterial nanomaterials exhibiting promising efficacy in the field, including their movement in the plant and their effect on bacteria at the micro- and nanoscale is critical. Invoking trans-disciplinary methods unlocks new ways to ascertain the mechanisms of action of the nanomaterials in plants. Monitoring minute changes taking place at the nanoscale, including morphology and chemical fingerprint, is expected to reveal new behaviors of biological systems that are not detectable with conventional analytical tools. In turn the multiscale analysis is likely to deepen the understanding of nanoparticles interaction with their environment.

Engineered zinc oxide-based nanotherapeutics boost systemic antibacterial efficacy against phloem-restricted diseases

Mikhael Soliman[1,2,°], Briana Lee[1,°], Ali Ozcan[1,3,‡,δ], Takat B. Rawal[4,5,#,δ], Mikaeel Young[1,6], Hajeewaka C. Mendis[1,7], Parthiban Rajasekaran[1], Torus Washington II[1], Sai Venkatesh Pingali[8], Hugh O'Neill[5,8], Andre Gesquiere[1,3], Leonardo De La Fuente[7], Loukas Petridis[4,5], Evan Johnson[9], James Graham[9], Swadeshmukul Santra[1,2,3,6]*, Laurene Tetard[1,10]*

[1] NanoScience Technology Center, University of Central Florida, Orlando, FL, 32826, USA
[2] Department of Material Science Engineering, University of Central Florida, Orlando, FL, 32816, USA
[3] Department of Chemistry, University of Central Florida, Orlando, FL 32816, USA
[4] UT/ORNL Center for Molecular Biophysics, Oak Ridge National Laboratory, Oak Ridge, TN, 37830
[5] Department of Biochemistry and Cellular and Molecular Biology, University of Tennessee, Knoxville,
[6] Burnett School of Biomedical Sciences, University of Central Florida, Orlando, FL 32816, USA
[7] Department of Entomology and Plant Pathology, Auburn University, Auburn, AL 36849
TN, 37996
[8] Neutron Scattering Division, Oak Ridge National Laboratory, Oak Ridge, TN, 37830
[9] Citrus Research and Education Center, University of Florida, Lake Alfred, Florida 33850, USA
[10] Department of Physics, University of Central Florida, Orlando, FL 32816, USA
[°] Equal contributions
[δ] Equal contributions
[‡] Current institution: Vocational School of Technical Sciences, Karamanoglu Mehmetbey University, Karaman, 70200, Turkey
[#] Present address: Department of Physics, University of Houston, Houston, TX, 77204

*Corresponding authors: swadeshmukul.santra@ucf.edu; laurene.tetard@ucf.edu

Keywords: nanotherapeutic, nanoagriculture, citrus greening, nanoscale imaging and spectroscopy, neutron scattering, antibacterial nanoparticle.

Abstract

Delivering active ingredients with high antibacterial efficacy at infected sites in plants is essential to reach the global goals for food security and sustainable agriculture productivity. Engineering nanomaterials is a suggested approach to attain systemic delivery of antibacterial active ingredients, thereby improving the efficacy of the treatments and minimizing harmful effects related to leaching in the environment. Herein, surface defect engineering of nanotherapeutics is used as a new form of active ingredient for systemic antimicrobial action in the phloem. The nanoparticle-based formulation, called Zinkicide®, features a spherical particle composed of a zinc oxide (ZnO) core and zinc peroxide (ZnO_2) shell with a total diameter below 5 nm. This formulation exhibits significant efficacy to manage citrus huanglongbing (HLB) disease as seen by the decrease in severity of symptoms and the increase from ~ 7% to 19% of medium and large fruits in HLB infected citrus groves, during field trials. Further analysis of the bacterial responses to Zinkicide® *in situ* indicates high potency at concentration as low as 9-18 μg/mL and biofilm growth inhibition at concentration of 50 μg/mL. Nanoscale infrared spectroscopy reveals morphology and secondary structure changes of the bacterial membrane upon treatment. The origin of the changes is considered, based on the optical signatures of the nanoparticles, indicative of surface defects. These inform a theoretical description of the participation of a ZnO_2/ZnO surface containing a pair of missing O atoms in the production of reactive oxygen species (ROS). The key participation of defects in the antibacterial action is confirmed experimentally by the slow decrease in antibacterial efficacy as nanoparticles age in media with passivation effects on the surface. This study reveals the importance of size and surface defects in the design of nanotherapeutics for targeted delivery and antibacterial activity.

Pathogens in food crops and feedstock constitute a significant threat to the food-water-energy security nexus, adding to the existing pressure of the growing population worldwide (1, 2). Challenges associated with global food production requirements (3, 4) to feed the 10.9 billion people projected in 2100 (5) are deeply intertwined with agricultural practices, environmental concerns, and new risks of disease emergence (1, 2, 6). Yet, disease management tools remain inadequate against numerous endemic plant diseases origination from bacteria, fungi or nematodes, which considerably hinders crop yields and increases the use of pesticides (7-11). Bacterial diseases are particularly challenging to manage. Current copper (Cu)-based and antibiotic-based treatments used in the field not only exhibit poor antimicrobial efficacy against new forms of bacterial resistance (10), but also prove to be ineffective in the treatment of bacterial infections situated in plant vascular tissues (11, 12). Trunk injection of the active ingredient, such as antibiotics, is being evaluated for phloem delivery (13, 14), though the technique is impractical for large scale deployment, and the widespread use of antibiotics can be concerning. Thermotherapy has also been studied but did not offer significant improvement in plant health in the long term (15). Overall, growers are left with limited option for the management of phloem-bound or xylem-bound pathogens. As a result, phloem-restricted pathogens will continue to have significant impacts on the crop yields of plants they target, with no effective treatment available to manage them. Left unaddressed, they may significantly hamper the sustainability of food production, which is particularly alarming in the context of a growing worldwide population.

Innovations in functional material engineering (16, 17), delivery systems (18) and sensing technologies (19, 20) have been relatively slow in the treatment of plant diseases, despite their potential to transform crop protection tools of high relevance to food-water-energy security deliverables. For instance, some engineered nanomaterials have been shown to provide superior bactericidal efficacy *in situ*, by increasing the bioavailability of active ingredients interacting with bacterial membranes (21-24), or by introducing modes of action that contrast from existing technologies such as Cu-products or antibiotics (25, 26). Yet, reports considering the field efficacy of engineered nanomaterial-based pesticides are infrequent (27). In addition, many countries have stringent processes for nanomaterial-based pesticide registration, which can impede their potential commercialization. Despite the hurdles associated with achieving large scale commercial use of nanomaterial-based bactericides for agriculture, they offer truly unique advantages, such as tunable dimensions, geometries, and surface chemistry. Thus, currently it is considered a tangible option to combat phloem- or xylem-restricted pathogens responsible for persistent plant diseases, as is the case for citrus greening, also known as Huanglongbing (HLB) (8, 28). HLB is a phloem-restricted bacterial disease associated to *Candidatus* Liberibacter asiaticus (*C*Las), which is decimating the citrus industry worldwide, due to the persisting lack of viable treatment (29-32). HLB has

results in global annual economic losses of billions of dollars (33). The rapid uptake and systemic mobility of nanoparticles below 100 nm observed in various plant systems (34), could bring about a paradigm shift in the treatment of vascular plant diseases, which remains to be explored.

It is well-established that the properties of nanomaterials are distinct from their bulk counterparts. For instance, catalytic properties can be observed in zinc oxide (ZnO) nanoparticles but not in larger particles (35, 36). ZnO nanoparticles also have interesting properties as catalysts (37). Nanocatalysts offer new avenues for catalysis, which is ubiquitous in industrial applications (38), including in agriculture for waste water remediation (39) or agri-food production (24, 40). Naturally-occurring catalysts are known to facilitate nutrient solubility in soils (41), while material engineering is used to produce oxidation catalysts for targeted applications such as water filtration (42), production of ammonia-based fertilizers (43), or formulation of stable and selective antibacterial agents (44, 45). In nanocatalysts, the presence of atomic surface defects acting as reaction centers is very appealing (46), especially thanks to the various avenues available to functionalize the surface of nanomaterials. Defects can introduce lower activation energy pathways that facilitate chemical reactions (47). As a result, defect-laden nanoparticle-based treatments are particularly potent *in situ*, including against multi-drug resistant bacteria (48-50) and viruses (51). Although mechanisms and modes of actions are not yet fully understood (52, 53), it has been suggested that the formation of reactive oxygen species (ROS) including hydrogen peroxide (H_2O_2) and hydroxyl radicals (·OH), which impact the cycle of cell development to cause cell death, contributing to the overall killing mechanism (54).

Here, we study the properties of the ZnO-based nanoparticles contained in the formulation, coined Zinkicide®, and their antibacterial efficacy *in situ* and *in planta*. We evaluate the effect of the treatment on tree health and fruit size in HLB-infected citrus trees. A comprehensive characterization of the nanoparticles is carried out to understand the properties contributing to the efficacy observed *in planta*. Structural and compositional analyses are supported by density functional theory (DFT)-based computational modeling. The effects of Zinkicide® on bacterial morphology, composition and on biofilm growth are evaluated with conventional bioassays and nanoscale infrared spectroscopy. Changes experienced by the nanoparticles aging in different environments are determined. The experimental evidence of the presence of surface defects on the nanoparticles leads to the development of computational DFT models to describe the mechanistic pathway of ROS generation at defect sites.

Materials and methods

ZnO nanoparticles synthesis:

A one pot wet synthesis method was used for the synthesis of Zinkicide® (55). 4.321 mg of Zinc nitrate hexahydrate powder (Fisher Scientific) was dissolved in 25 mL of DI water under continuous magnetic stirring at 400 rpm. Subsequently, 930 mg sodium salicylate (Alfa Aesar) was added to the Zn^{2+} solution to provide binding of salicylate to Zn and control the particle growth. The synthesis was completed by adding 3.33 mL of Hydrogen Peroxide (34% FG from Hydrite Chemical) into the solution, then raising the solution pH to 7.5 using 2 M $NaOH_{(aq)}$ (Fisher Scientific). The final volume of the sample was adjusted to 50 mL using DI water, and the concentration was calculated to be 19,000 μg/mL of Zn. pH was measured using a Delta 320 pH meter (Mettler Toledo), calibrated using commercial buffer solutions with known pH of 4, 7, and 10 (Fisher Science). 40 gallons of Zinkicide® were prepared for each field trial.

Zinkicide® nanoparticles were washed by centrifuging at 10,000 rpm for 5 min before decanting the supernatant and adding fresh DI water. The sample was vortexed and sonicated for 5 min to re-suspend the nanoparticles before the next round of washing. Each wash involved 10 repetitions of the previous steps.

To understand the mechanisms by which Zinkicide® offers such promise for canker and HLB treatments, compared to other standards such as Firewall or Nordox 30/30, we carried out a comprehensive analysis of the characteristics of the formulation.

Structure of the nanoparticles with electron microscopy:

High resolution Transmission Electron Microscopy (TEM): TEM measurements were carried out on freshly synthesized Zinkicide® solutions. Solutions were diluted to 250 μg/mL using DI water, then sonicated for 30 min before being drop-casted onto commercial TEM grids (CF-400-Au, Electron Microscopy Sciences). TEM images were acquired on a FEI Tecnai F30 microscope, with an electron beam intensity of 300 kV. Image analysis was carried out on the Gatan Microscopy Suite (GMS) 3 software.

Scanning Electron Microscopy (SEM) and elemental analysis: Freshly synthesized Zinkicide® solutions were prepared and drop-casted onto a freshly cleaned silicon wafer before sputter coating with gold-palladium (EMITECH sputter coater). Samples were then imaged using a ZEISS ULTRA-55 FEG SEM using the secondary electron detector. Multiple regions of samples were studied to determine the structure of the nanoparticles and their aggregation properties. The accelerating voltage used for imaging was 10 kV with a working distance of 13 mm. Elemental analysis, conducted concurrently with SEM

imaging, was performed using a Noran system 7 energy-dispersive x-ray spectroscopy (EDS) module with a silicon drift detector. The EDS spectral accuracy was verified by measuring the position of specific line intensities in the X-ray spectrum recorded with on reference SiO_2 and carbon-rich samples. This was used to screen for the presence evaluate the presence of Zinc in the various plant tissues. Data collection and analysis was performed using NSS software package.

Nanoparticle size with neutron scattering:

Small-angle neutron scattering (SANS) data was collected on the Bio-SANS instrument (CG3) at the High-Flux Isotope Reactor (HFIR) at the Oak Ridge National Laboratory (56). The instrument uses a passive collimation system of monochromatic cold neutron beam and a dual detector setup to access a wide dynamic q-range (Q ~ 0.003 to 0.85 $Å^{-1}$) in a single measurement. The main detector was placed at 15.5 m from the sample and the wing detector at 1.4° from direct beam. All measurements were performed using 6 Å neutron wavelength (λ) and 13.2% wavelength spread (Δλ/λ) and a sample aperture of 14 mm diameter placed at 17.48 m from the source aperture of 40 mm diameter. The processed SANS data used for analysis was obtained by correcting the raw SANS data for dark current, pixel sensitivity, solid angle and sample transmission prior to subtracting the scattering contribution of the background solvent.

Based on the composition of the Zinkicide® nanoparticles, we inferred that the nanoparticles as a whole would exhibit maximum contrast in 0% D_2O solvent, while at that 42% D_2O solvent would mask the surface coating making only the core is visible. As-synthesized Zinkicide® solutions were washed by placing 10 mL of the synthesized formulation in a semi-permeable cellulose membrane bag (MWCO 3.5 kD, Spectrum™ 132594) for dialysis. The wash was carried out with 4 L of DI water over a period of 72 h, refreshing the dialysis media every 8 h. The dialyzed solution was then freeze-dried before being redispersed at a high concentration (1 g/mL) in both 0% D_2O and 42% D_2O solutions, before being placed in titanium cells with detachable walls for ease of loading and unloading sample and mounted on a tumbler setup to prevent settling. Background signals including 0% D_2O and 42% D_2O were collected and subtracted from sample scattering prior to analysis. The SANS profiles were fit using the Unified fit approach(57, 58), especially useful for extracting hierarchical system structural features. The most relevant structural parameter is the primary particle diameter obtained from the high-Q region of the data. The relevant fit parameter is level-1 radius of gyration, R_g, which was converted to particle diameter, D (in Angstroms) assuming the particles are spherical (see supplementary information).

Chemical composition with Raman spectroscopy:

Raman spectra were acquired on a Alpha300 RA system (WITec) with excitation laser wavelength of 532 nm with output power of ~ 5 mW using a 10X objective. Silicon was used to ensure the relative Raman shift was located at 520 cm^{-1} before characterization of our solutions. Three 10 µL drops were casted on glass substrates for each solution. 100 spectra were acquired over a 100 μm^2 area on each drop to take into account variations across the drop. An integration time of 1 s per spectrum was used for spectra collection. For each measurements, 100 spectra were corrected with cosmic ray removal before being averaged and background corrected using the Project 4 software suite.

Nanoparticle size with dynamic light scattering (DLS):

100 µL of the stock solution was pipetted into a glass vial and filled with DI water to an adjusted final volume of 10 mL. The solution was then sonicated for ~ 1 min (Elmasonic S30H, Elma Schmidbauer GmbH) to completely disperse the particles. After sonication, 1.2 mL of the sample was pipetted into a clear disposable cuvette and placed in the DLS instrument (Zetasizer ZS90, He-Ne 632.8 nm, Malvern Panalytical). The instrument was set for dispersant DI water at 25ºC. The instrument attenuator used illumination laser power (4 mW). After an initial run was conducted, the samples were diluted as needed to obtain photon count rate between 100 kilo counts per second (kcps) and 300 kcps. Three subsequent measurements within range of the optimum conditions were collected and averaged to calculate the Z-average particle size.

Nanoparticle surface charges with Zeta potential:

Surface charges of the particles was studied using a Zetasizer (Malvern Zetasizer ZS90). Zeta potential (ζ) measurements were conducted on the same solutions as the ones used for size analysis. 0.75 mL of solution was pipetted into a Malvern zeta folded capillary cell (DTS1070) and placed inside the instrument. Program selections were identical to those chosen for size analysis. The sample values were tested and recorded for the determined optimal concentration (100-1000 kcps, 0.1 to 10 mS/cm). Three successive measurements within the range of optimal conditions were collected and averaged to determine the zeta potential.

Metal content with flame Atomic absorption spectroscopy (AAS):

The metallic zinc content of the Zinkicide® solutions was quantified with AAS (Perkin Elmer 400 AAS). 100 µL of Zinkicide® solution was placed into a 20 mL glass vial with 5 mL of aqua regia. The solution was stirred overnight in order to fully digest particles. After complete digestion, the volume was adjusted to 10 mL with DI water. Zinc standard solution concentrations spanning from 0.2 µg/mL to 2

μg/mL were prepared from a commercial AAS Zinc Standard solution of 1000 μg/mL for calibration. The first step of the measurement was carried out with a DI water blank to establish the background. The absorbance readings for standard solutions were recorded to form a standard calibration curve. Next, the digested samples were diluted with DI water to obtain the absorbance values corresponding to the standard calibration curve. The concentration of the initial stock solution was calculated using a linear conversion from the dilution factors. Each AAS was tested in triplicate.

Fluorescence and lifetime spectroscopy:

Fluorescence Lifetime Imaging (FLIM) was carried out with a custom-built fluorescence microscope(59) using a 373 nm pulsed diode laser (LDH-P-C-375, PicoQuant) excitation source at a repetition rate of 125 kHz. Photon arrival times were detected with a single photon avalanche diode (SPAD, PerkinElmerSPCM-AQR-14). For sample imaging, a cleaned glass slide was mounted onto the microscope and 50 μL of the formulation was transferred onto the substrate. The suspension was characterized in a liquid state within 5-10 min of application to the glass slide. Fluorescence intensity and FLIM data were collected simultaneously. FLIM images were captured with Symphotime software (Version 5.1.3.1, PicoQuant) synchronized with Labview (LabVIEW 9.0, National Instruments). After imaging, Time-Correlated Single Photon Counting (TCSPC) decay curves for each pixel in the FLIM image were tail fitted to determine the sample's lifetimes. All decay curves were fitted with bi-exponential functions and yielded τ_1 and τ_2 values reported herein.

Computational modeling:

For calculation of the Raman vibrational bands, three structural models were constructed: ZnO_2 bulk, ZnO_2(100) surface, and hybrid shell-core ZnO_2(100)/ZnO(10-10) system (see supplementary information). For the study of catalytic activity, a defective ZnO_2/ZnO hybrid with two missing O surface atoms was constructed. DFT calculations were performed using the QE package (60). The projector-augmented wave (PAW) pseudopotentials (61) were used to describe the electron-nuclei interaction. The plane wave basis set, with a kinetic energy cut-off of 634 eV (46.6 Ry) was employed. The geometry and frequencies of ZnO_2 systems were calculated with the PBEsol functional (62). The vibrational frequencies of the DFT-optimized structures were computed using the linear response approach within density functional perturbation theory (DFPT). To model non-local Van der Waals (vdW) interactions of adsorbates with the oxide surface, vdW-DF2-B86R (63) was implemented in QE (64). The usage of this functional made it possible to reproduce the experimentally established structural parameters for ZnO (47). Further details of our computation are provided in the supporting information. The energetics of the formation of ROS was evaluated by the energy difference (ΔE) between the pristine and defect-laden

systems with different adsorbates (H_2O_2, H_2O, O_2, OOH, and OH), where E is the DFT energy. The activation energy for a reaction on a representative nano ZnO surface was calculated using the climbing-nudged elastic band method (65).

Zn movement in plant:

Zn uptake by the plants was conducted using 5 phenotypically similar seedlings (6-month old greenhouse Young "Bitter Orange" (*Citrus* × *aurantium*) seedlings (~ 50 cm shoot length)) that were washed using DI water to remove residues from the greenhouse. 2 leaves from each plant were selected, placed into a 1 mL microcentrifuge tube containing 1 mL of Zinkicide® at 19,000 μg/mL (metallic content). The dose was selected to reach a level of nanoparticle uptake in the system that would be detectable with our characterization tools. UTC was placed in DI water. The leaves were kept in growth chamber for a total of 24 h with settings mimicking Florida grove conditions (temperature held between 25 °C and 31 °C, and humidity cycled between 60% and 80%). Seedlings experiments were conducted in a modified root uptake approach. The roots were carefully removed from the soil and thoroughly rinsed with DI water. They were then placed in 250 mL graduated cylinders filled with the treatment (150 mL of 19,000 μg/mL Zinkicide® for treated seedlings, DI water for UTC) for a total of 24 h in growth chamber set to mimic Florida grove conditions. The top of the graduated cylinder was sealed around the stem using parafilm to prevent evaporation. The graduated cylinder was wrapped in aluminum foil to maintain a dark environment of the treatment while in the chamber. After 24 h, the single leaves were collected and sectioned to retrieve the exudate for Raman spectroscopy measurement. In the case of the seedlings, leaves were separated from the stems. Stems were cross-sectioned at the approximate middle of the shoot. SEM with EDS measurements were conducted on the leaf and stem cross-sections. XRF measurements were carried out as described in the SI.

Antimicrobial efficacy:

Antibacterial efficacy of the formulations was determined using Gram-negative *E. coli* (ATCC 10536) and Gram-negative *Xanthomonas alfalfae* subsp. *citrumelonis* strain F1 (ATCC 49120, a citrus canker surrogate). Conventional minimum inhibitory concentration (MIC) assays using a broth microdilution method, as standardized by the Clinical and Laboratory Standards Institute (CLSI), were modified with resazurin dye to improve detection. Kanamycin, a standard antibiotic, was used at a concentration of 50 μg/ml as the positive control for killing. After 24 h of incubation at 37° C, 10 μL of resazurin dye (0.0125 % w/v) per 100 μL/well was added to provide visualization of inhibition efficacy via color changes (blue to pink for live organisms).

After MIC determination, a range of concentrations (31-500 μg/mL) were selected for further quantification using colony forming units (CFU) assays. As per CLSI requirements, a culture concentration of 0.5 McFarland standards was used as a starter culture for all the bacterial species, from which $1x10^5$ CFU/well (final concentration $5x10^5$ CFU/ml) was added, as previously described.(66) Bacteria were treated using the same formulations and following the same procedure as the one described for the MIC assay. Each sample was serially diluted in 1X PBS and plated on nutrient or LB agar at 26 or 37ºC. After 24 or 48 h of incubation, individual colonies were counted and CFU/mL quantified. All measurements were done in triplicate.

Microfluidic chambers:

Fabrication of microfluidic chambers (MC) was performed as previously described by De La Fuente *et al*.(67) MC experiments were set up as described in Mendis *et al.* (68) for evaluation of biofilm formation of *Xanthomonas citri* subsp. *citri* (Xcc) strain 306. Xcc was grown at 28°C with shaking at 150 rpm in Silva Buddenhagen (SB) (69) broth or on SB agar plates. Briefly, MC used in the experiments consisted of two parallel-channels, 80 μm wide, 3.7 cm long and 50 μm deep. Each channel in the MC has two inlets to introduce media and bacteria and one outlet to remove all the liquid flowing in the channel. All the inlets and outlets were connected to tubing, syringes and syringe pumps (Pico Plus; Harvard Apparatus, Holliston, MA, USA) as described by De La Fuente *et al.* (67) Xcc bacteria suspensions were introduced to both MC channels and media flow was set to 0.05 μL/min. Introduction of Xcc cells to MC was stopped after 2-3 hours, when enough Xcc cells were attached to the MC glass surface. Attached Xcc cells formed biofilms for 3 days, then SB medium with 50 μg/mL Zinkicide® (metallic Zn content) was introduced only to the top channel after Xcc formed biofilm in both channels. Nikon Eclipse Ti inverted microscope (Nikon, Melville, NY) with phase-contrast and Normarski differential interference contrast (DIC) optics was used to observe MC, and time-lapse images were recorded every 1 min for 240 min with a Nikon DS-Q1 digital camera (Diagnostic Instruments, Sterling Heights, MI, USA) connected to the microscope and controlled by NIS-Elements imaging software.

Atomic Force Microscopy and nano-IR spectroscopy:

Bacterial samples were prepared by collecting 1 mL aliquots of recently grown stationary phase *Xanthomonas alfalfae* subsp. *citrumelonis* strain F1. Samples were a 1:1 mixture of bacteria and treatment (DI water for control) which were incubated at 28 °C for 2 h. Bacteria were treated with a) Cu hydroxide at 250 μg/mL (control), b) Cu_2O/ZnO at 125 μg/mL(Cu)/125 μg/mL(Zn) (control), c) as-synthesized Zinkicide® at 38 μg/mL, and d) washed Zinkicide® at 130 μg/mL and were compared to untreated control incubated in growth media. For rinsing, bacteria were centrifuged at 5000 rpm for 5 min to pellet. The

supernatant was discarded, and the pellet was resuspended in 500 μL of ddH_2O. This washing process was repeated 3 times to remove residues for infrared spectroscopy and nanoscale imaging measurements. For imaging, silicon wafers were cut into squares, and thoroughly cleansed by sonicating for 20 min each in acetone, ethanol, and DI water, then dried with compressed air.

Bacteria topography was imaged in contact mode (scan rate 1 Hz) using a NanoIR2 AFM (Bruker Nano Surface, Santa Barbara, CA, USA). Nanoscale infrared spectra and chemical maps at selected wavenumbers of the same bacteria were collected. All images were obtained under ambient conditions (23°C, ~35% relative humidity) using silicon n-type cantilevers coated with gold on both sides (model: PR-EX-nIR2-10, nominal resonance frequency of 13 ± 4 kHz, spring constant of 0.07-0.4 N/m). For nano-IR measurements, the laser pulse was tuned at a contact resonance of the cantilever. Spectra were collected by monitoring the variation in amplitude of the contact resonance as a function of wavenumber in the range 1740-1580 cm^{-1} at a fixed location. Chemical maps were acquired by fixing the wavenumber, 1650 cm^{-1} for the images displayed here, while nano-IR spectra (N ≈ 75 for each treatment) were collected using a step size of 2 cm^{-1}. Images collected were further analyzed using Anasys Analysis, OriginLab 2017, and Fityk 1.3.1.

Greenhouse and field trials:

The systemic movement and efficacy of Zinkicide® were evaluated using soil drench and spray application on canker-infected citrus trees, obtained by leaf inoculations of bacterial pathogen *Xanthomonas citri* subsp. *citri* (Xcc) (SI Section S2) (Fig. 1a). Greenhouse canker bioassays were performed as previously described (70), with slight modification of the treatment application. The former study focused on screening the efficacy of earlier formulation of valence-engineered ZnO nanoparticles against citrus Canker. Briefly, 'Pineapple' sweet orange (*Citrus sinensis*) seedlings grown in 4000 cm^3 containers in Metro Mix 500 (Hummert International, Earth City, MO) soilless medium and fertilized with 10 g of controlled release granular fertilizer (18-5-10; Harrell's, Lakeland, FL). Uniform seedlings with approximately 1 cm stem caliper were cut back so that only two dominant shoots were allowed to develop. At about 25-50% leaf expansion on three to four leaves of each shoot, treatments were applied. In the case of spoil drench application, treatments (100 and 400 μg/mL) were applied to run through. In the case of foliar application, the entire plant was treated by applying the treatment with an airbrush (Crown Spra-Tool, Aervoe Industries, Inc., Gardnerville, NV) at 10 ml per seedling. Runoff into the soilless medium was minimized at that stage. One day after treatment applications five seedlings per treatment were inoculated with 10^4 CFU/ml of *X. citri* subsp. c*itri* strain X2002-0014 in PBS buffer. The bacterial suspension was injection-infiltrated in three panels on each side of the midrib to six distinct inoculations per leaf on three to four leaves per replicate seedling. Inoculated shoots were covered with plastic bags to maintain humidity and

randomly distributed on a bench in an air-conditioned greenhouse with 28/25°C day/night temperatures. Plastic bags were removed after 1 day. Lesions were counted at each inoculation site and summed as lesions per leaf at 14 days post inoculation. The efficacy was evaluated by the percent decrease in lesion numbers following treatment of inoculated leaves, compared to untreated control (UTC) and control treated with translaminar streptomycin-based standard (Firewall 17WP from Agrosource, Inc.) using 18 mg of product per plant.

Field evaluation of Zinkicide against HLB was done on a subset of treatments in a citrus canker trial previously described (70). Doses of 100 and 400 μg/mL were evaluated via soil drench or foliar spray, as described in the Results. Fruit quality and HLB disease rating data was taken in November 2015 after two years of treatment to the experimental plots with 10 foliar sprays per year at 21-day intervals from March to October. One hundred fruit per plot were harvested and sized on a Color Vision System (CVS) fruit sizing line at the University of Florida Citrus Research and Education Center. Visual disease rating was performed independently by two people on a scale of 1=no symptoms, 2=leaf symptoms present, 3=mild decline, 4=moderate decline, 5=severe decline or death. Decline was considered a combination of leaf drop (canopy thinning) and branch dieback.

Statistics were conducted using Proc GLM with SNK means separation in SAS 9.4.

Results and discussion

Green house and field efficacy for canker and HLB

Large quantities of Zinkicide®, a formulation containing engineered ZnO nanoparticles, were synthesized for field trials (~ 40 gallons per field trial, see methods in Supplementary Information (SI)). Application of Zinkicide® formulation in greenhouse and field settings showed significant improvements in the health and yield of canker- and HLB-infected citrus trees (Figure 1). The reduction of canker lesions on the leaves up to ~55% was observed compared to UTC after soil drenching of 400 μg/mL (metallic Zn content) Zinkicide® (Fig. 1a), which surpasses the performance of Firewall (~80% of lesions remaining compared to UTC). The soil drenching with 100 μg/mL Zinkicide® did not show any reduction in the number of lesions, whereas foliar spray of Zinkicide® exhibited significant reduction of the lesions at both 100 and 400 μg/mL concentration (Fig. 1a). Zinkicide® applied by spray or soil drench at 400 μg/mL showed equivalent efficacy (~ 60%) (Fig. 1a). This indicates that the delivery of Zinkicide® is systemic in citrus trees and present antibacterial activity above a threshold concentration.

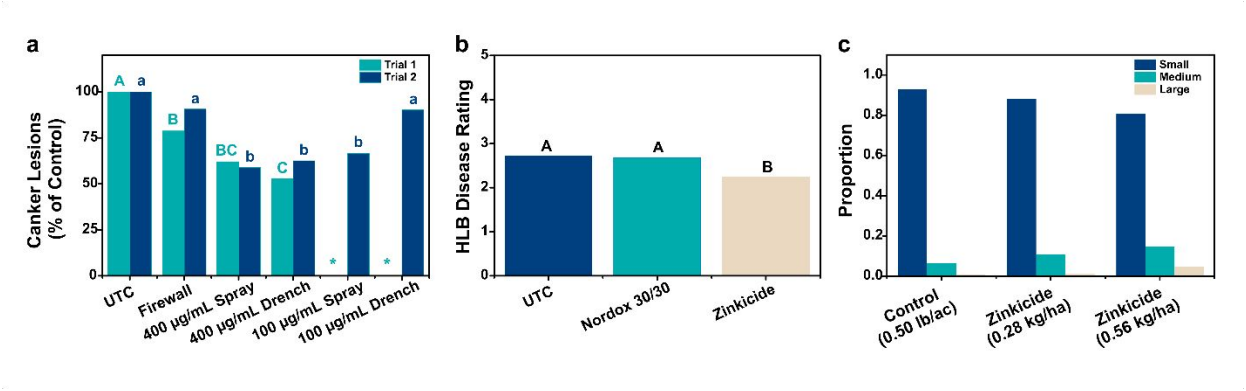

Fig. 1 a, Effect of concentration (100 µg/mL, and 400 µg/mL Zinkicide®) and application methods (root drench vs. foliar spray) on canker lesion reduction as % of lesions formed on untreated control (UTC) leaves for two trials (* = treatments excluded from Trial 1). Treatments were compared to UTC and translaminar streptomycin-based Firewall. Statistical analysis was carried out for SNK means separation. **b,** Efficacy of Zinkicide® in mitigating visual HLB disease symptoms compared to untreated (UTC) and Nordox 30/30 (standard insoluble copper with equal amount of Zinc oxide) treated HLB-affected citrus. HLB disease rating of 1 = no symptom present, 2 = sectored symptoms present, 3 = mild decline, 4 = moderate decline, 5 = severe decline/death was used. Statistical analysis was carried out for SNK means separation. **c,** Distribution of grapefruit size collected after treatment with Zinkicide® (0.28 kg/ha and 0.56 kg/ha) compared with a control of citrus canker trial Nordox 30/30 (containing 0.56 kg/ha of ZnO). The control was selected to avoid any bias caused by canker induced fruit drop. Size categories are based on diameters for commercial fruit per box: small (56-64 fruits per box), medium (40-48 fruits per box), and large (32-36 fruits per box).

Improvements in HLB symptoms were observed in field trials carried out in HLB-affected groves (SI Section S2). Visual disease rating of trees treated with Zinkicide® showed a significant decrease in symptoms severity, with a rating of 2, corresponding to sectored symptoms (Fig. 1b). UTC and Nordox 30/30 (mixture of cuprous oxide/zinc oxide)-treated trees both rated at ~2.7, corresponding to signs of mild decline of the trees. Though signs of the disease were still visible on the leaves, a decrease in symptoms severity from ~2.7 to ~2.1 is currently not achievable without trunk injection of antibiotics (71). The distribution of grapefruit size after Zinkicide® treatment indicated a significant increase in the proportion of medium (from ~6% to ~14%) and larger fruits (from <1% to ~5%) (Fig. 1c), which are commercially valuable and extremely difficult to obtain on HLB-affected trees. Increasing the amount of Zinkicide® used from 0.28 kg/ha (ZnO) to 0.56 kg/ha (ZnO) further improved the proportion of medium and large fruits. The efficacy of Zinkicide® *in planta* is in agreement with prior work reporting the antimicrobial effect of nano-zinc oxide -2S albumin protein formulation on growth of *C*Las *in planta* (72).

Structure and composition of Zinkicide®

Transmission electron microscopy (TEM) revealed aggregates of nanoparticles (Fig. 2a) with polycrystalline orientation (Fig. 2c) in the deposits of Zinkicide®. Scanning electron microscopy (SEM) images of the air-dried formulations corroborate the TEM observations (SI section S3, Fig. S1). Individual nanoparticles with a diameter between 2.5 and 5 nm were observed with high resolution TEM (Fig. 2b and Fig. S2). Fast Fourier Transform (FFT) analysis of the single nanoparticles confirmed their crystalline nature, with five distinctive lattice fringes supporting the assignment to a ZnO wurtzite structure (JCPDS Card No. 36-1451) (Table S1). Small-angle neutron scattering (SANS) also confirmed significant agglomeration in the suspension of a high concentration of Zinkicide® particles in water, with a hierarchical structure extending over multiple length scales (Fig. 2d and SI section S3). The most notable feature was found in the high-Q region (> 0.1 $Å^{-1}$), which is related to the Zinkicide® primary particle shape, size, and the low degree of order in their arrangement (*i.e.,* not random). The nanoparticles were suspended in two different H_2O/D_2O ratios of aqueous solvents to highlight, respectively, the entire core-shell structure of the particles (0% D_2O solvent) and only their cores (42% D_2O). Analysis of the SANS spectra (SI Section S3, Table S2) revealed an average core of the particles of 2.7 nm with a shell thickness of at most 0.4 nm (Fig. 2d), in good agreement with the TEM findings.

The composition of the nanoparticles found in Zinkicide® was confirmed using Raman spectroscopy (Fig. 2e, Figure S3). The signature of the as-synthesized formulation containing all excess reagents exhibited bands corresponding to sodium salicylate (818 cm^{-1} bending mode of C-C, 1020 cm^{-1} in-plane bending mode of C-H, 1260 cm^{-1} stretching mode of C-O in hydroxyl group, 1390 cm^{-1} stretching mode of C-O in carboxyl group, 1460 cm^{-1} stretching mode of C-C, 1630 cm^{-1} stretching mode of C=O, and 3070 cm^{-1} stretching mode of C-H) (73), nitrate (1050 cm^{-1} and 1360 cm^{-1} symmetric and antisymmetric stretching modes of the nitrate ion, respectively) (74), and hydrogen peroxide (870 cm^{-1} stretching mode of O-O) (75). To evaluate the properties of the nanoparticles without excess reagents, the solution was thoroughly washed (see methods in SI) and resuspended in DI water. The corresponding Raman spectrum reveals a band at 840 cm^{-1} corresponding to the stretching mode of O-O, likely in a form of ZnO_2 (76) (inset in Fig. 1e). The presence of this band was not evident in the spectrum of the as-synthesized formulation due to the dominating signal of excess hydrogen peroxide at 870 cm^{-1}.

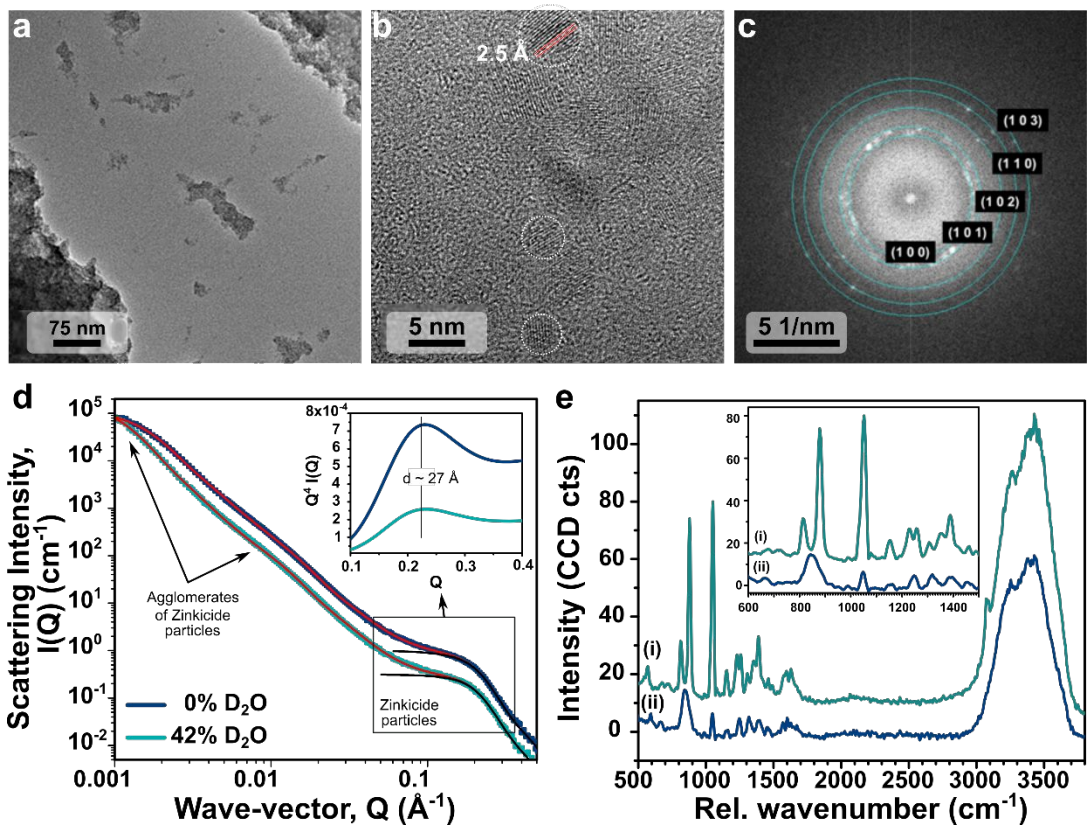

Fig. 2 a, TEM image of Zinkicide® aggregates. **b**, High resolution TEM image of ZnO nanoparticles demonstrating their ultra-small size between 2.5 nm and 6 nm. **c**, FFT analysis of the TEM image in **b** revealed lattice d-spacings of Zinkicide® corresponding to ZnO Wurtzite (JCPDS: 36-1451). **d,** Small-angle neutron scattering of Zinkicide® particles in 0% (blue dots) and 42% (green dots) D_2O solvents. Total Unified fit (red solid line) consists of 3 levels of structural regimes (black line represents individual Zinkicide® particles). Inset: Inter-particle distance (peak) highlighted by plotting the porod plot- $Q^4I(Q)$ vs. Q of the primary structural level. **e,** Raman spectra of (i) as synthesized (unwashed) Zinkicide® and (ii) washed Zinkicide® in DI water. Inset: fingerprint region (500-1500 cm^{-1}) unveiling the presence of ZnO_2 in the nanoparticles with representative band at 840 cm^{-1}.

The chemical species corresponding to the Raman-active vibration at 840 cm^{-1} was confirmed by calculating, using density functional perturbation theory, the O-O stretching frequencies of three structural model systems: (i) ZnO_2 bulk (Fig. S4a,b), (ii) ZnO_2 (100) surface (Fig. S4c), and (iii) hybrid shell-core system of a ZnO_2 surface monolayer supported by ZnO with three layers, constructed to mimic a nanoparticle with a ZnO core and a ZnO_2 surface (Fig. S5). A change in O-O bond length, $d_{(O-O)}$, was noted between the bulk (1.46 Å), the ZnO_2 surface (1.49 Å), and the shell-core hybrid (1.51 Å). This resulted in a O-O stretching frequency of 873 cm^{-1} for the bulk ZnO_2, 860 cm^{-1} for the ZnO_2-(100) surface, and 837 cm^{-1} for the shell-core ZnO_2/ZnO system (Table S3), supporting our experimental evidence that the shell of the nanoparticles is made of ZnO_2.

To understand one possible mechanism of the formation of the ZnO_2 surface monolayer, we modeled, with DFT, a defective (77) ZnO (10-10) surface, with a single O vacancy interacting with H_2O_2. The model shows that H_2O_2 adsorbs at a surface Zn site near an O vacancy with an adsorption energy of -1.02 eV. We calculated the reaction pathway for the reaction $H_2O_2^* \rightarrow OOH^*_{(O\text{-}vac)} + H^*_{(O\text{-}surf)}$, where * indicates an adsorbed species and found it to be energetically favorable by 0.55 eV with an activation energy of 0.41 eV (~16 k_BT) (Fig. 3a-c). In the dissociated state, $H^*_{(O\text{-}surf)}$ adsorbs at a surface O atom and $OOH^*_{(O\text{-}vac)}$ occupies the O vacant site (Fig. 3c). The reaction, $OOH^* \rightarrow O_2^*_{(O\text{-}vac)} + H^*_{(O\text{-}surf)}$, which yields the bound O_2 species on the nano surface (Fig. 3d-f), is slightly exothermic ΔE = -0.05 eV and has an activation energy of 0.29 eV. After dissociation, O_2 adsorbs at the vacancy site with one O atom attached to a surface Zn atom while the other O occupies the vacant site. The H atom adsorbs at a surface O atom (Fig. 3f). The $H_2O_2^* \rightarrow OOH^*_{(O\text{-}vac)} + H^*_{(O\text{-}surf)}$ reaction constitutes the rate-limiting step with a relatively high barrier. Overall, the DFT calculations suggest that surface defects facilitate the formation of bound O_2 on the ZnO surface, which may serve as a precursor of the ZnO_2 surface layer observed in Zinkicide®.

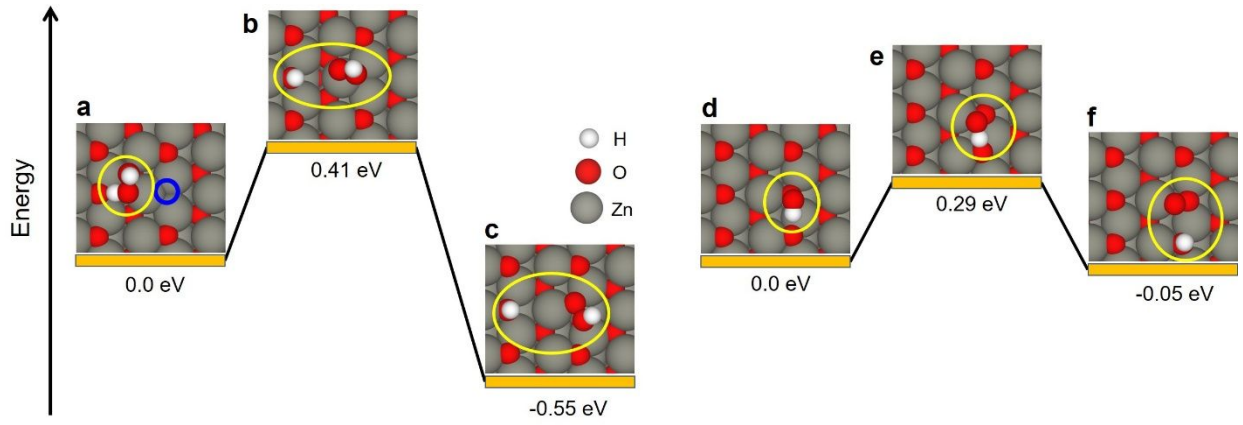

Fig. 3 DFT energy profile for the dissociation of **a-c**, hydrogen peroxide (H_2O_2) and **d-f**, hydroperoxyl (OOH) on a defective ZnO(10-10) surface with an O vacancy (shown by the blue circle). **a,** Initial state consisting of a H_2O_2 adsorbed at a surface Zn site near the O vacancy. The energy of the system is set as reference energy. **b,** Transition state with an activation energy of 0.41 eV. **c,** Final state, where H adsorbs at a surface O atom and OOH adsorbs at an O vacancy site. This process is exothermic with ΔE = -0.55 eV. **d**, Initial state, where OOH adsorbs at an O vacancy site. **e**, Transition state with an activation energy of 0.29 eV. **f**, Final state, where H adsorbs at surface O atom and oxygen molecule adsorbs at the vacancy site. The process is slightly exothermic with ΔE = -0.05 eV. The energy on the vertical axis is not shown to scale.

Movement of ZnO nanoparticles in citrus

Uptake of Zinkicide® via the roots was confirmed by analyzing the Raman signature of leaf exudates from root-treated citrus seedlings (Fig. 4b and SI Section 5, Fig. S3). After 24 h of exposing the seedling roots to the formulation, Zn nitrate was found in leaves exudates (Figure S3). A notable band at 1060 cm^{-1} corresponding to nitrate indicates that the formulation translocated from the roots to the leaves via the xylem, as depicted in Fig. 4a. Elemental analysis, using SEM and energy dispersive x-ray spectroscopy (EDS), was carried out on cross-sections of the midrib to probe the pith, inner and outer xylem, and the phloem (Fig. 4c,d). In all regions of the treated plant cross sections, except the pith, a band at 1.01 keV corresponding to the Zn L_α transition was observed. However, this band was absent in the same regions of the untreated plant cross sections (Fig. S7). SEM images of the vasculature (Fig. 4c, Fig. S7) revealed the presence of nanoparticle-like features with a strong Zn signal at 1.01 keV in several vascular channels (Fig. S7). Additional quantitative studies showed that it is possible to tune the Zn concentration delivered to the phloem and xylem of the seedlings treated with Zinkicide® to levels above 2000 µg/g (Fig. S8).

The observations are in agreement with a study by Etxeberria *et al.*, which demonstrated that nanoparticles with diameters below 5 nm exhibit improved uptake by plant leaves followed by their systemic movement after treatment (78). Uptake of nanoparticle of different size up to several hundred nanometers in diameter through soil drench application has also been previously reported (79). However, smaller nanoparticles are expected to have a better propensity for systemic movement (78). Furthermore, engineered micronutrient-based nanoparticles with biocompatible coatings have been found to prevent plant tissue damage and phytotoxicity, and have beneficial effects on plants (80), which agrees well with our observations. However, to remain potent *in planta*, the treatment in the system should be delivered at the infected sites at a concentration above the minimum inhibitory concentration (MIC).

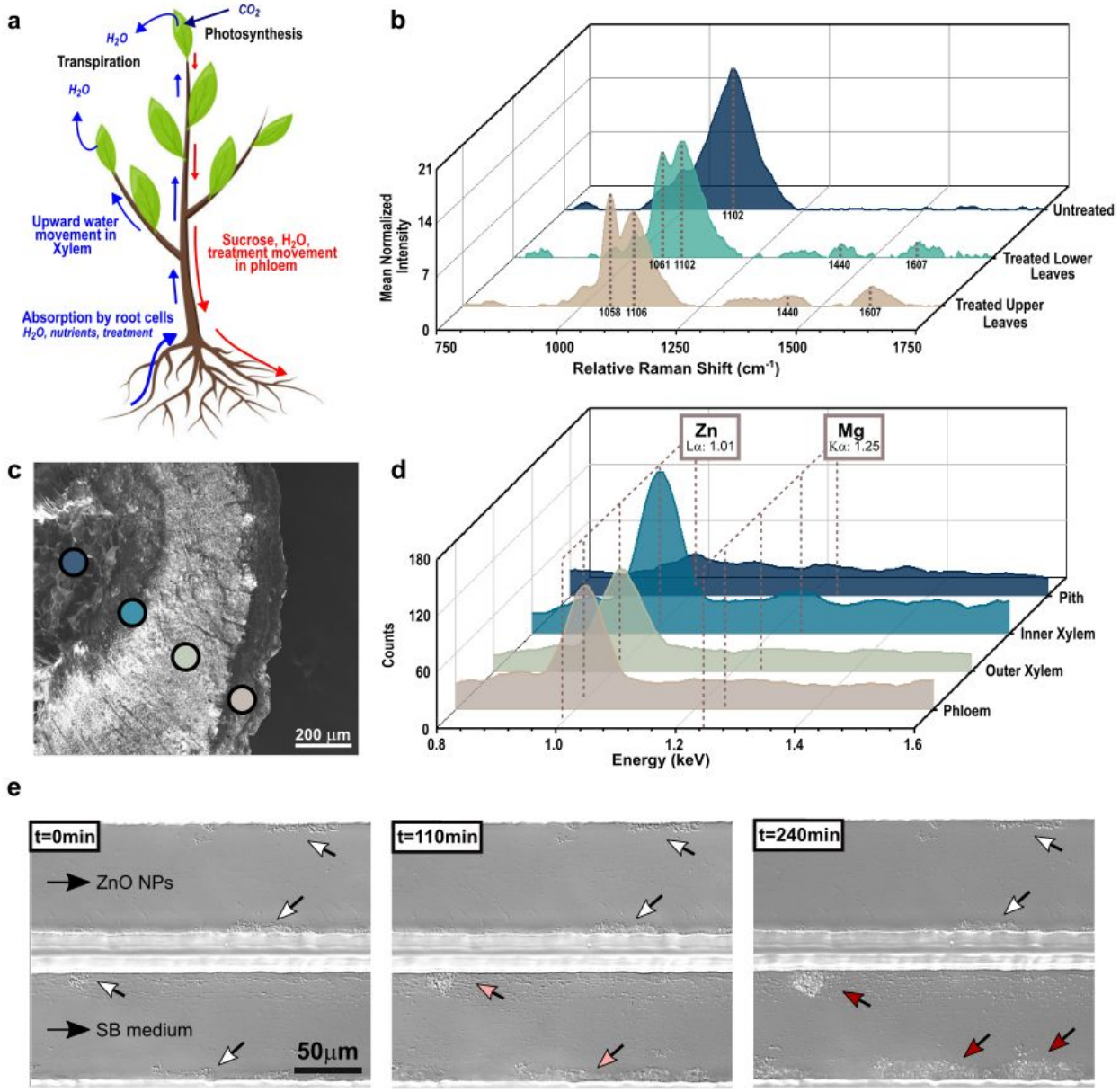

Fig. 4 a, Schematic representation of conventional translocation in the plant after root uptake. **b**, Raman spectra of leaf exudates from untreated seedlings, and from leaves collected in the upper and lower foliage of treated seedlings. **c**, SEM of leaf midrib cross-section. **d,** Corresponding EDS spectra collected in the pith, inner xylem, outer xylem and phloem, as marked in **c**. **e**, Modeling of the growth of *Xanthomonas citri* subsp. *citri* (Xcc) biofilm growth in presence of Zinkicide® using microfluidic channels. Growth of Xcc biofilm monitored under constant flow (0.05µL/min) of SB medium with Zinkicide® (50 µg/mL, noted ZnO NPs) (top channel) and SB medium only (bottom channel).

Effect of ZnO nanoparticles on bacteria

As Zinkicide® uptake studies confirmed that high levels of Zn in the vascular system of the plants can be achieved (Fig. S8), we investigated the minimum concentration required to inhibit bacterial and biofilm growth. *C*Las biofilms formed in the phloem as a result from HLB infections cannot currently be cultured *in vitro* (81). Instead, we evaluated the antibacterial efficacy of freshly synthesized Zinkicide® on *X. alfalfae* and *E. coli* using standard bioassays *in vitro* (Table 1, Fig. 5) and its inhibiting effect on biofilms using the citrus pathogen Xcc in a microfluidic platform (Fig. 4e) (68, 82, 83). Zinkicide®, as formulated, inhibited growth at 9-18 μg/mL (metallic Zn content) against *E. Coli* and 38 μg/mL (Zn content) against *X. alfalfae* (Table 1). The MICs of copper hydroxide (Kocide) and cuprous oxide/ZnO (Nordox 30/30) controls observed at 250-500 μg/mL (metallic Cu content) and 125-250 μg/mL (Cu:Zn content), respectively. This corresponds to a ~14-fold improvement in lowering MIC when using Zinkicide® compared to controls for *E. coli*, and a ~3-fold improvement for *X. alfalfae.*

We evaluated the effect of Zinkicide® in conditions that mimic the vascular system using a microfluidic channel, as described in a recent study (84) (See Methods). As seen in the images presented in Fig. 4e, the presence of Zinkicide® (top channel) disrupted the growth of the Xcc biofilm. Partial removal of the biofilm was observed compared to the growth of Xcc biofilm in the control medium (bottom channel), as shown by the red arrows in the middle and right panels. However, we note that some of the biofilm remained in the channel for the conditions considered, suggesting that further optimization of the concentration and frequency of application should be considered to reach the MIC required to fully inhibit *C*Las *in planta*.

We also investigated the effect of replacing excess reagents with water on the antimicrobial efficacy of the remaining ZnO nanoparticles. The MIC (Table 1) and colony-forming unit (CFU) (Fig. 5c,d) measurements indicate a loss of efficacy when treating with the ZnO nanoparticles dispersed in water (labeled Zinkicide® in water in Table 1 and Fig. 5), although their potency remained higher than that of cuprous oxide/zinc oxide (Nordox 30/30) and copper hydroxide (Kocide) for *E. coli.* For *X. alfalfae*, the nanoparticles in water exhibited a MIC similar to the cuprous oxide/zinc oxide (Nordox 30/30) control, but higher than copper hydroxide (Kocide). CFU assays (Fig. 5c,d) confirmed that the efficacy of ZnO nanoparticles is comparable to industry standards but lower than as-synthesized Zinkicide®. A trend of efficacy loss could also be noted over the course of the 18-weeks aging process.

Table 1. *E. coli* and *X. alfalfae* minimum inhibitory concentrations (MIC). MIC values reported for the nanoparticles as-synthesized with excess of reagents (Zinkicide® as-synthesized), after removal of reagent excess (Zinkicide® in water) and controls for week 1 to 4 after synthesis.

Antimicrobial agent activity on *E. coli*	***MIC Range (µg/mL)***			
	Week 1	**Week 2**	**Week 3**	**Week 4**
Zinkicide® as-synthesized	9 – 18	9 – 18	9 – 18	9 – 18
Zinkicide® in water	32 – 65	260	260	260
Copper hydroxide (Kocide)	250 – 500	250 – 500	250 – 500	250 – 500
Cuprous oxide/zinc oxide (Nordox)	125 – 250 (Cu): 125 – 250 (Zn)	125-250 (Cu): 125-250 (Zn)	125-250 (Cu): 125-250 (Zn)	125-250 (Cu): 125-250 (Zn)
Antimicrobial agent activity on *X. alfalfae*	***MIC Range (µg/mL)***			
	Week 1	**Week 2**	**Week 3**	**Week 4**
Zinkicide® as-synthesized	38	38	38	38
Zinkicide® in water	130 – 260	260 – 520	260 – 520	260 – 520
Copper hydroxide (Kocide)	250 – 500	250 – 500	250 – 500	250 – 500
Cuprous oxide/zinc oxide (Nordox)	125 – 250 (Cu): 125 – 250 (Zn)	125-250 (Cu): 125-250 (Zn)	125-250 (Cu): 125-250 (Zn)	125-250 (Cu): 125-250 (Zn)

Next, we evaluated the effect of the treatment on the morphology and composition of individual *X. alfalfae* bacteria using atomic force microscopy (AFM) and nanoscale infrared spectroscopy (nano-IR) (85-87) (Fig. 5e-g). Topography AFM images of individual bacteria (Fig. 5e) revealed significant changes in size, shape, and roughness of the cell membranes compared to the untreated *X. alfalfae*, especially for bacteria treated with Zinkicide®. Nano-IR spectra, in the 1720-1580 cm^{-1} range, were collected at various locations across the bacteria and on several bacteria. Spectra, representative of the signature for each treatment, are presented in Fig. 5f. The band observed with maximum amplitude ~1660 cm^{-1} corresponds to the amide I vibration in the bacterial cell (88). Deconvolution of the amide I band was used to estimate the contribution of β-turns (~1710 cm^{-1}), random coil (~1660 cm^{-1}) and β-sheets (~1625 cm^{-1}) (89). The findings indicate that different treatments affected the percentage of secondary structural features of proteins in the cell wall. Small position shifts were observed, which could be due to the local relative humidity of the samples during imaging. The relative amplitude of the bands revealed a change in secondary structure, specifically for Zinkicide®. β-sheets made up ~25% of the signature of untreated *X. alfalfae.* Treatments with Nordox and as-synthesized Zinkicide® increased the amount to ~30-35%. On the other hand, treatments with Kocide and Zinkicide® nanoparticles in water led to a decrease to 18%

and 0.1%, respectively. Although these do not translate directly to the quantity of β-sheets in the bacteria, they indicate a change in secondary structure, potentially denaturation of the proteins.

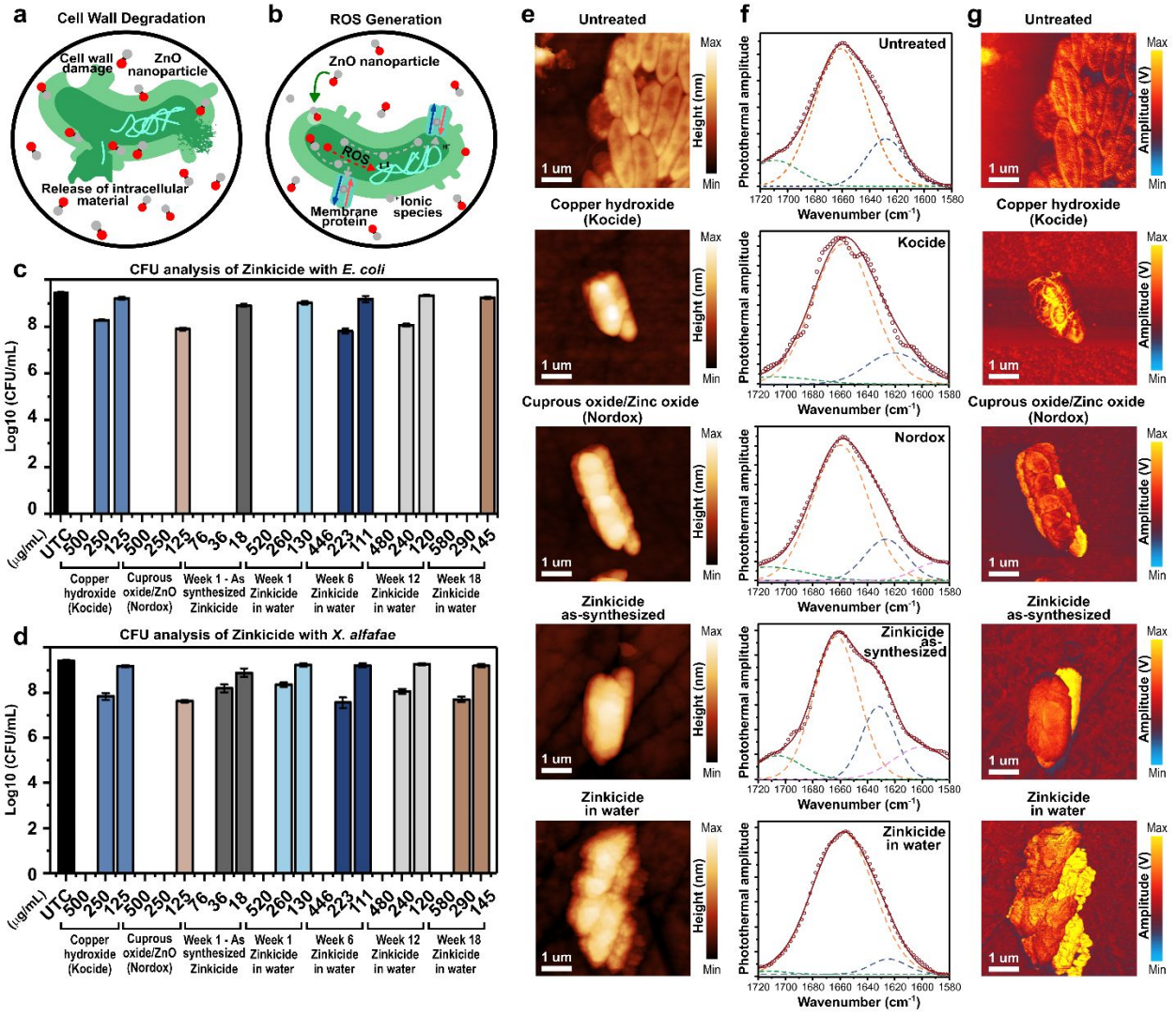

Fig. 5 a, **b,** Antibacterial mode of actions of Zinkicide®, including **a**, cell wall degradation, and **b,** ROS generation. **c,** CFU analysis of antimicrobial efficacy of 1-week old as-synthesized Zinkicide® nanoparticles compared to copper hydroxide, cuprous oxide/zinc oxide, and ZnO nanoparticles in water at weeks 1, 6, 12, and 18 on *E. coli*. **d,** CFU analysis of antimicrobial efficacy of 1-week old as-synthesized Zinkicide® nanoparticles compared to copper hydroxide, cuprous oxide/zinc oxide, and ZnO nanoparticles in water at weeks 1, 6, 12, and 18 on *X. alfalfae.* **e,** AFM height images with **f,** corresponding nano-IR spectra and **g,** chemical maps (1650 cm^{-1}) of *X. alfalfae* untreated, and treated with copper hydroxide (Kocide), cuprous oxide/zinc oxide (Nordox), as-synthesized Zinkicide® and Zinkicide® in water.

Additional details of the bands are listed in Table S5. The corresponding chemical maps (Fig. 5g), obtained by fixing the laser wavelength (1650 cm^{-1}) to excite random coil vibrations in the cell and by

measuring the resulting photothermal expansion across the sample with the AFM probe, suggest that chemical heterogeneities appear in the cells for all treatments. However, the variations are distributed across the membranes treated with Kocide, while changes were found in specific regions (yellow regions) in the bacteria treated with Nordox. Images of Zinkicide®-treated cells indicated that changes occurred in some bacteria but not others. We note that the morphological aspect of all bacteria treated with Zinkicide® nanoparticles in water (no excess reagents) were affected more significantly than with any other treatment suggesting that direct contact with the nanoparticles does play a role in the activity of the treatment. Such heterogeneities cannot be captured with conventional infrared spectroscopy.

Transformation of Zinkicide® nanoparticles over time

We studied the physical traits and antibacterial efficacy of the nanoparticles after aging in reagents versus aging in water (referred to as washed in SI) in ambient conditions over the course of 18 weeks. Dynamic light scattering (DLS) measurements indicate that the size of the nanoparticle aggregates (Fig. S9) remained constant for 18 weeks. At week 1 hydrodynamic diameters of ~ 159 ± 23 nm and 170 ± 18 nm were obtained for as-synthesized Zinkicide® and for Zinkicide® in water, respectively, while respective diameters of 164 ± 14 nm and 173 ± 3 nm were measured at week 18 (Fig. S9a). Surface charges of as-synthesized Zinkicide® did not experience any statistical change, with a Zeta potential of ~ -12.5 (± 9) mV at week 1 and ~ -17.1 (± 11) mV at week 18 (Fig. S9b). On the other hand, the potency of as-synthesized Zinkicide® remained constant for the first five weeks despite minor fluctuations (Table S4), followed by a noticeable decay in antibacterial activity at week 6 against *X. alfalfae*. The loss in efficacy was only observed at week 18 against *E. coli* (Table S4). Control treatments (copper hydroxide (Kocide) and cuprous oxide/zinc oxide (Nordox30/30)) exhibited constant, though poorer, performance than as-synthesized Zinkicide®. Zinkicide® nanoparticles aging in water showed efficacy either superior or comparable to that of copper hydroxide (Kocide), for both bacterial strains considered.

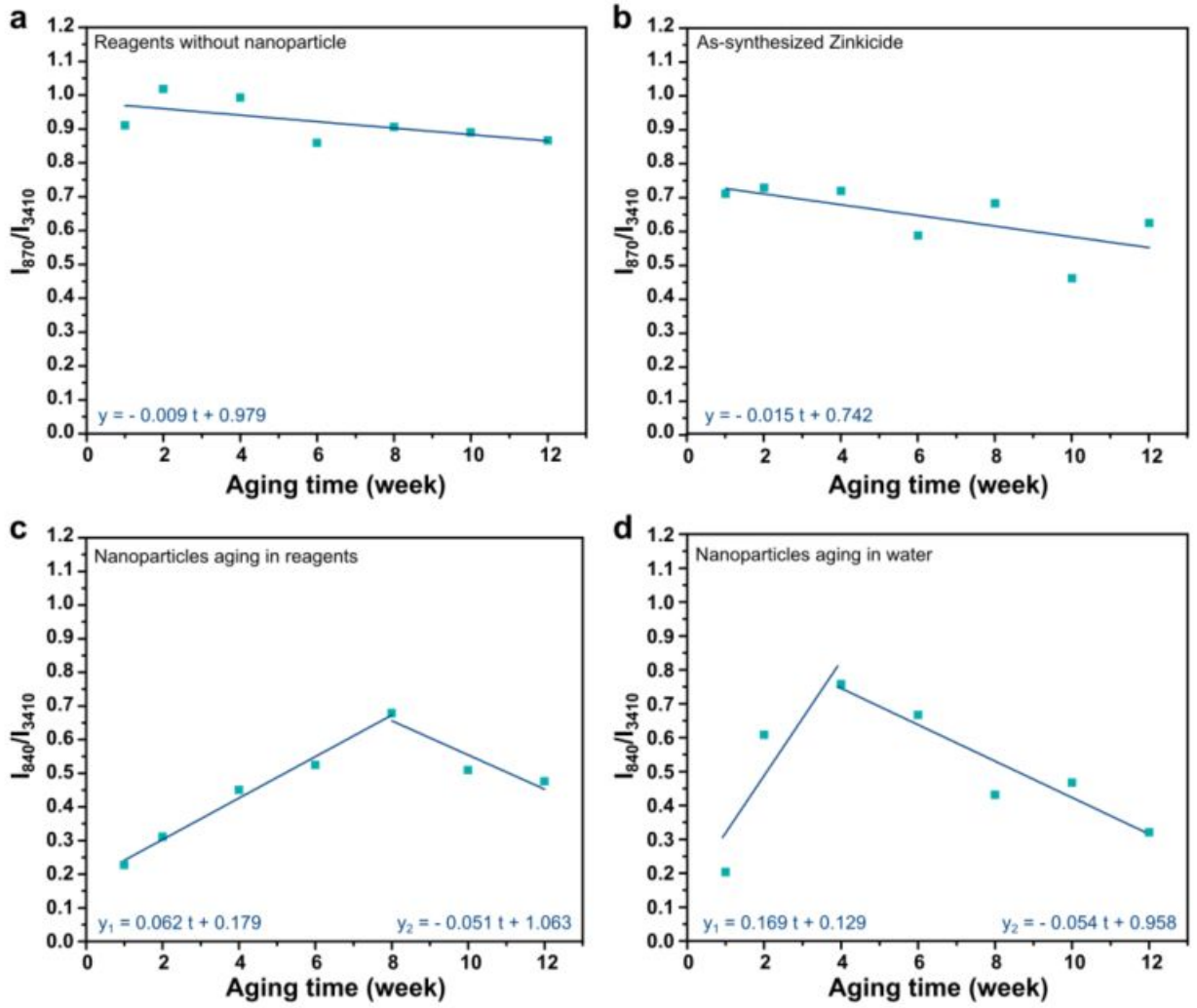

Fig. 6 Evolution of the hydrogen peroxide to water content evaluated from the Raman intensity ratio I_{870}/I_{3410} of **a,** reagents without nanoparticles and **b,** as-synthesized Zinkicide® over 12 weeks. Evolution of the zinc peroxide of the nanoparticle shell to water content over 12 weeks evaluated using the Raman intensity ratio I_{840}/I_{3400} of **c,** nanoparticles aging in reagents with excess reagents removed and suspended in water at the time of measurement, and **d,** nanoparticles with excess reagents removed from as-synthesized Zinkicide® on week 1, followed by continued aging in water. The solid lines represent estimated linear trends of the experimental data.

Next, we investigated the evolution of the solution composition accompanying the changes in antibacterial efficacy. The hydrogen peroxide content in the aging as-synthesized Zinkicide® was assessed by monitoring the ratio of the characteristic hydrogen peroxide Raman band intensity at 870 cm^{-1} to the water band intensity at 3410 cm^{-1}, labeled I_{870}/I_{3410} (Fig. 6b), from Raman spectra presented in Fig. S10. The ratio varied from ~ 0.70 to ~ 0.55 during the first 12 weeks. The slope of the decay was steeper than that of the control solution containing all excess reagents without the ZnO nanoparticles (Fig. 6a), which

remained constant around 0.9. The slight decrease observed for the control solution is attributed to some evaporation during storage in ambient conditions, while the larger decrease of as-synthesized Zinkicide® (Fig. 6b) is attributed to a reaction at the surface of the nanoparticles, which is consistent with the DFT calculations (Fig. 3) and the antibacterial efficacy of as-synthesized Zinkicide® (Table S4). When considering the evolution of the nanoparticles aged in reagents as in the case in as-synthesized Zinkicide® but focusing on the nanoparticles themselves (Fig. 6c), the ratio of the intensity of the Raman ZnO_2 band at 840 cm^{-1} to the intensity of the 3410 cm^{-1} water Raman band (I_{840}/I_{3410}) reaches a maximum at week 8. This suggests that the reaction of hydrogen peroxide with the nanoparticle surface defect sites, described in Fig. 3, evolves until a maximum content of ZnO_2 is reached at week 8, followed by a decay in nanoparticle efficacy, which correlates well with the slight loss of efficacy observed around week 6 against *X. alfalfae*. For the nanoparticles aged in water (Fig. 6d and Table S4), we observed an increase in I_{840}/I_{3410} for the first four weeks, likely due to a reaction between the defects of the ZnO_2 shell and water. Similarly, immediately after removing excess reagents, the MIC against *E. coli* decayed from 32-45 μg/mL in week 1 to 270 μg/mL after week 4. Against *X. alfalfae* the MIC remained constant from week 2 to 12 at 260-520 μg/mL. This suggests that the particles did not dissolve during the 12 weeks of the study but experienced changes to the reactivity of the ZnO_2 shell. Correspondingly, a low amount of Zn was found in water with Atomic Absorption Spectroscopy (AAS) between week 1 to 12 (Fig. S11). Fluorescence lifetime imaging measurements (FLIM) (Fig. S12) revealed that as-synthesized Zinkicide® nanoparticles consistently returned relatively short lifetimes (τ_1 and τ_2 values), with none exceeding 9 ns for the 18-week period considered (Table S6). The shorter lifetime component dominated, with a much larger amplitude than the τ_2 component (Table S6). However, after the first two weeks of aging, maximum laser power (800-850 nW) was required to collect sufficient counts/sec (Table S7). Control solutions without nanoparticles were characterized and did not exhibit any fluorescence. Although the qualitative yield of emission appears lower over time, the consistency of the excited state lifetime data suggests that the ZnO core of the particles remained intact, while the loss of radiative recombination is due to the changes taking place in the environment of surface defects. Potential processes taking place at surface defects and their role in the evolution of the antibacterial efficacy of the formulation are discussed hereafter.

Catalytic properties of ZnO nanoparticles

We explored the catalytic properties of ZnO and ZnO_2/ZnO surfaces with defects (Fig.7). Using DFT, we evaluated the energetics of the reactions of selected adsorbates on the surface of a defective surface monolayer of ZnO_2 with two missing O atoms, supported by ZnO (Fig. 7b), consistent with the shell-core model identified from the Raman spectra (Fig. 2e) and DFT model (Fig. 7a) indicating that

ZnO facilitates the formation of a peroxide overlayer. The adsorbates considered were those potentially involved in surface-catalyzed generation of ROS: H_2O_2, H_2O, O_2, OOH, and OH. Taking the adsorbed $H_2O^*+O_2^*$ as a reference state (Fig. 7c), the reaction $H_2O^* + O_2^* \rightarrow OH^* + OOH^*$ was found to be endothermic (ΔE=+0.30 eV, Fig. 7d), while the reaction $H_2O^* + O_2^* \rightarrow OH^* + OH^* + O^*$ was exothermic (ΔE=-1.13 eV, Fig. 7e). Thus, bound hydroxyls were identified as the energetically favorable ROS on the defective ZnO_2/ZnO system.

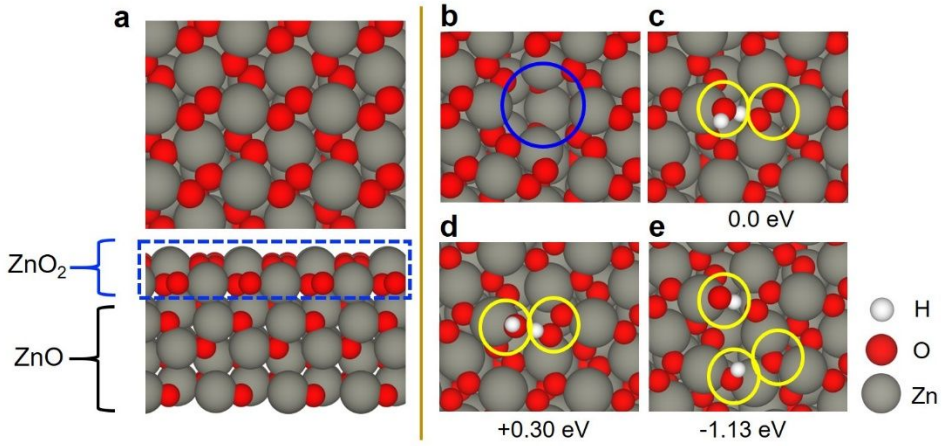

Fig. 7. a, DFT structural model of shell-core ZnO_2/ZnO system (Top panel: top view; bottom panel: side view). The ZnO_2 surface monolayer (blue dashed line) is supported by ZnO(10-10) (side view). **b**, Defective ZnO_2/ZnO system containing a pair of missing O atoms. **c-e,** DFT-optimized geometries, and relative energetics of binding of adsorbates on the defective ZnO_2/ZnO shell-core system. **c,** O_2^* and H_2O^*; **d,** OOH* and OH*; **e,** OH*, OH* and O*. The values given in eV, represent the difference in DFT-calculated energy (ΔE) relative to a configuration shown in **c** and (*) represents the adsorbed species. The configuration shown in **e** has the lowest DFT energy.

Our DFT model shows that the defects, *i.e.,* the oxygen vacancies, serve as the binding sites for the oxygen atoms of the adsorbates, and therefore play an important role for surface-catalyzed ROS (OH*, O*) generation (Fig. 3c and 3f, Fig. 7e). Hence nano-ZnO_2 and ZnO (54, 90) surfaces can serve as active components for the antibacterial formulation. The changes in chemical signatures and morphology of the bacteria observed with nano-IR seem to support this inference as ROS have been reported to affect the structural conformation of proteins in bacteria (91).

Conclusion

We demonstrated the superior efficacy of Zinkicide®, a sub-5 nm ZnO-based nanoparticle as an active nanotherapeutic, to combat HLB disease in citrus groves. The ability to manufacture the product in

large quantities using a one-pot synthesis method enabled greenhouse and field trials, which showed reduction of the leaf canker lesions when applied to the root system. This strong evidence of systemic movement from roots to leaves was further confirmed by in-depth characterization of the treated plant tissues. Notably, SEM images and elemental analysis detected the presence of Zn-rich nanoparticles in the phloem and xylem after Zinkicide® treatment. Consistently low levels of Zn ion released in water under the conditions considered suggests that the nanoparticles, rather than Zn ions, are systemically delivered *in planta*.

An important study moving forward will be the evaluation of the MIC of Zinkicide® on *C*Las, followed by in-depth analyses of nanoparticle-bacteria interactions to identify the mechanisms of action. However, this effort is currently on hold due to the challenges associated with *in vitro* culture and manipulation of *C*Las. Despite this limitation, *in vitro* measurements were carried out on model systems and confirmed the high antibacterial efficacy and biofilm growth inhibition efficacy of Zinkicide® compared to common growers' standards. Considerations of the evolution of Raman spectra, MIC, AAS and fluorescence lifetime data collected on Zinkicide® aging for up to 18 weeks converge to suggest that modification of the nanoparticle surface is a more probable cause of the observed loss in efficacy over time than a dissolution of the nanoparticles. DFT calculations indicate that surface defects play an important role in the generation of ROS that can contribute to biocidal reactions. More specifically, the oxygen vacancies serve as the binding sites for the oxygen atoms of the adsorbates, participating in surface-catalyzed ROS (OH*, O*) generation. Treatment of the bacteria model systems with Zinkicide® resulted in morphological and structural changes confirmed by nanoscale imaging and spectroscopy. A change in secondary structure, potentially denaturation of the proteins due to ROS, was noted as well as the fact that not all bacteria were affected by the treatments the same way.

Based on the observations of *in situ* and greenhouse trials, the lack of efficacy observed when treating citrus trees by soil drench with Zinkicide® at 100 μg/mL could be due to a dilution of the treatment in the tree before it reaches the necessary sites. Optimizing concentration and frequency of application should be considered to ensure the systemic delivery of Zinkicide® to infected phloem channels is done above MIC levels, for greater impact on plant health. We showed that treating seedlings with higher concentration of Zinkicide® (19000 μg/mL) resulted in Zn content up to 7000 μg/g delivered to the plant. Hence, dilution effect should be taken into account when translating studies from seedlings to larger trees for field trials. The density of defect sites at the surface of the nanoparticles, and their ability to remain catalytically active to interact with bacteria *in planta* will be critical to maintain to maintain high efficacy of the treatment over long periods of time. Nevertheless, the demonstrated efficacy against canker and symptoms of HLB in the present study (i.e., Zinkicide® applied at 400 μg/mL) remains significantly superior to what can be achieve with growers 'standards currently used in the field. Despite

the promising efficacy of Zinkicide®, further challenges related to regulatory concerns lie ahead. This will require, for instance, a more general assessment of the environmental impacts such a new active would have as a commercial product.

Associated content

The Supporting Information is available, including the methods and additional figures and tables.

Acknowledgements

The authors acknowledge the support of the National Institute of Food and Agriculture, U.S. Department of Agriculture, under award number USDA Grant 2015-70016-23010 and the Citrus Research and Development Foundation (project # 907) for this study. This research used resources of CADES at the Oak Ridge National Laboratory, which is supported by the Office of Science of the U.S. Department of Energy under Contract No. DE-AC05-00OR22725, and at the High Flux Isotope, a DOE Office of Science User Facility operated by the Oak Ridge National Laboratory.

M. Soliman and B. Lee contributed equally to this work. A. Ozcan and T. B. Rawal contributed equally to this work. A. Ozcan acknowledges current affiliation, Vocational School of Technical Sciences, Karamanoglu Mehmetbey University, Karaman, 70200, Turkey. T. B. Rawal acknowledges current affiliation, Department of Physics, University of Houston, Houston, TX, 77204.

Author contributions

A.O., M. Y. and S. S. designed and synthesized the nanomaterials. E. J. performed the field trials. E. J., J. G. and S. S. interpreted the field data and identified Zinkicide as the material of interest for the comprehensive study. M. S., A. O., M. Y., P. R. and L.T. carried out the measurements pertaining to the nanomaterial characterization. M. S. carried out the measurements pertaining to the movement of the nanoparticles in plants. B. L., M. Y., H. M., and P.R. carried out the measurements pertaining to the nanoparticle-bacterial interactions. B.L. carried out the nanoscale infrared measurements. H.M. and D.L. carried out the microfluidic measurements. W. T. and A. G. carried out the fluorescence and lifetime measurements. T. R. carried out the DFT calculations. L. T., S.S., A. O. and L. P. supported the neutron scattering measurements carried out and analyzed by S. V. P. and H. O.. All authors participated in the preparation and correction of the manuscript.

References

1. Rohr JR, Barrett CB, Civitello DJ, Craft ME, Delius B, DeLeo GA, et al. Emerging human infectious diseases and the links to global food production. Nature Sustainability. 2019;2(6):445-56.
2. Wang D, Saleh NB, Byro A, Zepp R, Sahle-Demessie E, Luxton TP, et al. Nano-enabled pesticides for sustainable agriculture and global food security. Nature Nanotechnology. 2022;17(4):347-60.
3. Finley JW, Seiber JN. The Nexus of Food, Energy, and Water. Journal of Agricultural and Food Chemistry. 2014;62(27):6255-62.
4. Scanlon BR, Ruddell BL, Reed PM, Hook RI, Zheng C, Tidwell VC, et al. The food-energy-water nexus: Transforming science for society. Water Resources Research. 2017;53(5):3550-6.
5. World Population Prospects: 2019 Revision, United Nations. http://esa.un.org/unpd/wpp/; 2019.
6. Baker RE, Mahmud AS, Miller IF, Rajeev M, Rasambainarivo F, Rice BL, et al. Infectious disease in an era of global change. Nature Reviews Microbiology. 2022;20(4):193-205.
7. Gottwald TR, Graham JH. Citrus diseases with global ramifications including citrus canker and huanglongbing. CAB Reviews: Perspectives in Agriculture, Veterinary Science, Nutrition and Natural Resources. 2014;9:016.
8. Mansfield J, Genin S, Magori S, Citovsky V, Sriariyanium M, Ronald P, et al. Top 10 plant pathogenic bacteria in molecular plant pathology. Molecular Plant Pathology. 2012;13(6):614-29.
9. Sundin GW, Wang N. Antibiotic resistance in plant-pathogenic bacteria. Annual review of phytopathology. 2018;56:161-80.
10. Sundin GW. Antibiotic Resistance Affects Plant Pathogens. Science. 2001;291(5513):2551-.
11. Bendix C, Lewis JD. The enemy within: phloem-limited pathogens. Molecular Plant Pathology. 2018;19(1):238-54.
12. Sundin GW, Castiblanco LF, Yuan X, Zeng Q, Yang C-H. Bacterial disease management: challenges, experience, innovation and future prospects: Challenges in Bacterial Molecular Plant Pathology. Molecular plant pathology. 2016;17(9):1506-18.
13. Hu J, Jiang J, Wang N. Control of Citrus Huanglongbing via Trunk Injection of Plant Defense Activators and Antibiotics. Phytopathology®. 2017;108(2):186-95.
14. Hijaz F, Nehela Y, Al-Rimawi F, Vincent CI, Killiny N. The Role of the Xylem in Oxytetracycline Translocation within Citrus Trees. Antibiotics (Basel). 2020;9(10):691.
15. Vashisth T, Livingston T. Efficacy of In-field Thermotherapy in Comparison and Combination of Defoliation for Mitigating Huanglongbing in Sweet Orange. HortScience horts. 2020;55(2):251-7.
16. Scott N, Chen H. Nanoscale science and engineering for agriculture and food systems. Industrial Biotechnology. 2013;9(1):17-8.
17. Huang B, Chen F, Shen Y, Qian K, Wang Y, Sun C, et al. Advances in Targeted Pesticides with Environmentally Responsive Controlled Release by Nanotechnology. Nanomaterials. 2018;8(2):102.
18. Santra S, Rajaraman S, Lee WH, Yunjun X, CAMPOS MGN. Phloem-based delivery of therapeutics. Google Patents; 2019.
19. Baek S, Jeon E, Park KS, Yeo K, Lee J. Monitoring of Water Transportation in Plant Stem With Microneedle Sap Flow Sensor. Journal of Microelectromechanical Systems. 2018;27(3):440-7.
20. Church J, Lee WH. A novel approach for in situ monitoring of Zn2+ in citrus plants using two-step square-wave anodic stripping voltammetry. MRS Communications. 2018;8(2):404-10.
21. Kim DY, Kadam A, Shinde S, Saratale RG, Patra J, Ghodake G. Recent developments in nanotechnology transforming the agricultural sector: a transition replete with opportunities. Journal of the Science of Food and Agriculture $V 98. 2018(3):849-64.
22. Banik S, Pérez-de-Luque A. In vitro effects of copper nanoparticles on plant pathogens, beneficial microbes and crop plants. 2017. 2017;15(2).
23. Singh A, B Singh N, Hussain I, Singh H, Singh S. Plant-nanoparticle interaction: An approach to improve agricultural practices and plant productivity2015. 2319-6718 p.

24. Singh RP, Handa R, Manchanda G. Nanoparticles in sustainable agriculture: An emerging opportunity. Journal of Controlled Release. 2021;329:1234-48.
25. Ismail M, Prasad R, Ibrahim AI, Ahmed AI. Modern prospects of nanotechnology in plant pathology. Nanotechnology: Springer; 2017. p. 305-17.
26. Ocsoy I, Tasdemir D, Mazicioglu S, Tan W. Nanotechnology in Plants. In: Varshney RK, Pandey MK, Chitikineni A, editors. Plant Genetics and Molecular Biology. Cham: Springer International Publishing; 2018. p. 263-75.
27. Worrall EA, Hamid A, Mody KT, Mitter N, Pappu HR. Nanotechnology for Plant Disease Management. Agronomy. 2018;8(12).
28. Kurepa J, Paunesku T, Vogt S, Arora H, Rabatic BM, Lu J, et al. Uptake and Distribution of Ultrasmall Anatase TiO_2 Alizarin Red S Nanoconjugates in Arabidopsis thaliana. Nano Letters. 2010;10(7):2296-302.
29. Ghosh D, Motghare M, Gowda S. Citrus Greening: Overview of the Most Severe Disease of Citrus. Advanced Agricultural Research & Technology Journal. 2018;2(1):83-100.
30. Kumar P, Kesari P, Kokane S, Ghosh DK, Kumar P, Sharma AK. Crystal structures of a putative periplasmic cystine-binding protein from Candidatus Liberibacter asiaticus: insights into an adapted mechanism of ligand binding. The FEBS Journal. 2019;286(17):3450-72.
31. Kumar P, Dalal V, Sharma N, Kokane S, Ghosh DK, Kumar P, et al. Characterization of the heavy metal binding properties of periplasmic metal uptake protein CLas-ZnuA2†. Metallomics. 2019;12(2):280-9.
32. Ma W, Pang Z, Huang X, Xu J, Pandey SS, Li J, et al. Citrus Huanglongbing is a pathogen-triggered immune disease that can be mitigated with antioxidants and gibberellin. Nature Communications. 2022;13(1):529.
33. Singerman A, Rogers ME. The Economic Challenges of Dealing with Citrus Greening: The Case of Florida. Journal of Integrated Pest Management. 2020;11(1):3.
34. Tripathi DK, Shweta, Singh S, Singh S, Pandey R, Singh VP, et al. An overview on manufactured nanoparticles in plants: Uptake, translocation, accumulation and phytotoxicity. Plant Physiology and Biochemistry. 2017;110:2-12.
35. Nair MG, Nirmala M, Rekha K, Anukaliani A. Structural, optical, photo catalytic and antibacterial activity of ZnO and Co doped ZnO nanoparticles. Materials Letters. 2011;65(12):1797-800.
36. Manohar A, Park J, Geleta DD, Krishnamoorthi C, Thangam R, Kang H, et al. Synthesis and characterization of ZnO nanoparticles for photocatalysis, antibacterial and cytotoxicity in kidney cancer (A498) cell lines. Journal of Alloys and Compounds. 2021;874:159868.
37. Siddiqi KS, Ur Rahman A, Tajuddin, Husen A. Properties of Zinc Oxide Nanoparticles and Their Activity Against Microbes. Nanoscale Res Lett. 2018;13(1):141-.
38. Wijngaarden RI, Westerterp KR, Kronberg A, Bos A. Industrial catalysis: optimizing catalysts and processes: John Wiley & Sons; 2008.
39. Anjum M, Miandad R, Waqas M, Gehany F, Barakat MA. Remediation of wastewater using various nano-materials. Arabian Journal of Chemistry. 2016.
40. Sekhon BS. Nanotechnology in agri-food production: an overview. Nanotechnology, Science and Applications. 2014;7:31-53.
41. Morgan JB, Connolly EL. Plant-Soil Interactions: Nutrient Uptake. Nature Education Knowledge. 2013;4(8):2.
42. Li D, Qu J. The progress of catalytic technologies in water purification: A review. Journal of Environmental Sciences. 2009;21(6):713-9.
43. Anderson JS, Rittle J, Peters JC. Catalytic conversion of nitrogen to ammonia by an iron model complex. Nature. 2013;501:84.
44. Cai L, Chen J, Liu Z, Wang H, Yang H, Ding W. Magnesium Oxide Nanoparticles: Effective Agricultural Antibacterial Agent Against Ralstonia solanacearum. Frontiers in Microbiology. 2018;9(790).
45. Elmer W, Ma C, White J. Nanoparticles for plant disease management. Current Opinion in Environmental Science & Health. 2018;6:66-70.

46. Behrens M, Studt F, Kasatkin I, Kühl S, Hävecker M, Abild-Pedersen F, et al. The Active Site of Methanol Synthesis over $Cu/ZnO/Al_2O_3$ Industrial Catalysts. Science. 2012;336(6083):893.
47. Rawal TB, Ozcan A, Liu S-H, Pingali SV, Akbilgic O, Tetard L, et al. Interaction of Zinc Oxide Nanoparticles with Water: Implications for Catalytic Activity. ACS Applied Nano Materials. 2019;2(7):4257-66.
48. Malka E, Perelshtein I, Lipovsky A, Shalom Y, Naparstek L, Perkas N, et al. Eradication of multi-drug resistant bacteria by a novel Zn-doped CuO nanocomposite. Small. 2013;9(23):4069-76.
49. Slavin YN, Asnis J, Häfeli UO, Bach H. Metal nanoparticles: understanding the mechanisms behind antibacterial activity. Journal of Nanobiotechnology. 2017;15(1):65.
50. Goyal B, Verma N, Kharewal T, Gahlaut A, Hooda V. Structural effects of nanoparticles on their antibacterial activity against multi-drug resistance. Inorganic and Nano-Metal Chemistry. 2022:1-13.
51. Sharmin S, Rahaman MM, Sarkar C, Atolani O, Islam MT, Adeyemi OS. Nanoparticles as antimicrobial and antiviral agents: A literature-based perspective study. Heliyon. 2021;7(3):e06456.
52. Ingle AP, Duran N, Rai M. Bioactivity, mechanism of action, and cytotoxicity of copper-based nanoparticles: A review. Applied Microbiology and Biotechnology. 2014;98(3):1001-9.
53. Sondi I, Salopek-Sondi B. Silver nanoparticles as antimicrobial agent: a case study on E. coli as a model for Gram-negative bacteria. Journal of Colloid and Interface Science. 2004;275(1):177-82.
54. Lakshmi Prasanna V, Vijayaraghavan R. Insight into the Mechanism of Antibacterial Activity of ZnO: Surface Defects Mediated Reactive Oxygen Species Even in the Dark. Langmuir. 2015;31(33):9155-62.
55. Rawal TB, Smith MD, Ozcan A, Smith JC, Tetard L, Santra S, et al. Role of Capping Agents in the Synthesis of Salicylate-Capped Zinc Oxide Nanoparticles. ACS Applied Nano Materials. 2020;3(10):9951-60.
56. Heller WT, Urban VS, Lynn GW, Weiss KL, O'Neill HM, Pingali SV, et al. The Bio-SANS instrument at the High Flux Isotope Reactor of Oak Ridge National Laboratory. Journal of Applied Crystallography. 2014;47(4):1238-46.
57. Beaucage G. Approximations Leading to a Unified Exponential/Power-Law Approach to Small-Angle Scattering. Journal of Applied Crystallography. 1995;28(6):717-28.
58. Beaucage G. Small-Angle Scattering from Polymeric Mass Fractals of Arbitrary Mass-Fractal Dimension. Journal of Applied Crystallography. 1996;29(2):134-46.
59. He J, Towers A, Wang Y, Yuan P, Jiang Z, Chen J, et al. In situ synthesis and macroscale alignment of CsPbBr(3) perovskite nanorods in a polymer matrix. Nanoscale. 2018;10(33):15436-41.
60. Giannozzi P, Andreussi O, Brumme T, Bunau O, Buongiorno Nardelli M, Calandra M, et al. Advanced capabilities for materials modelling with Quantum ESPRESSO. J Phys: Condens Matter. 2017;29(46):465901.
61. Blochl PE. Projector Augmented-Wave Method. Phys Rev B 1994;50(24):17953-79.
62. Perdew JP, Ruzsinszky A, Csonka GI, Vydrov OA, Scuseria GE, Constantin LA, et al. Restoring the density-gradient expansion for exchange in solids and surfaces. Phys Rev Lett. 2008;100(13):136406.
63. Hamada I. van der Waals density functional made accurate. Physical review B, Condensed matter. 2014;89(12):121103.
64. Thonhauser T, Zuluaga S, Arter CA, Berland K, Schroder E, Hyldgaard P. Spin Signature of Nonlocal Correlation Binding in Metal-Organic Frameworks. Phys Rev Lett. 2015;115(13):136402.
65. Henkelman G, Uberuaga BP, Jónsson H. A climbing image nudged elastic band method for finding saddle points and minimum energy paths. The Journal of Chemical Physics. 2000;113(22):9901-4.
66. Rajasekaran P, Santra S. Hydrothermally Treated Chitosan Hydrogel Loaded with Copper and Zinc Particles as a Potential Micronutrient-Based Antimicrobial Feed Additive. Frontiers in Veterinary Science. 2015;2(62).
67. De La Fuente L, Burr TJ, Hoch HC. Mutations in Type I and Type IV Pilus Biosynthetic Genes Affect Twitching Motility Rates in <em>Xylella fastidiosa</em&gt. Journal of Bacteriology. 2007;189(20):7507.

68. Mendis HC, Ozcan A, Santra S, De La Fuente L. A novel Zn chelate (TSOL) that moves systemically in citrus plants inhibits growth and biofilm formation of bacterial pathogens. PLOS ONE. 2019;14(6):e0218900.
69. Mongkolsuk S, Loprasert S, Whangsuk W, Fuangthong M, Atichartpongkun S. Characterization of transcription organization and analysis of unique expression patterns of an alkyl hydroperoxide reductase C gene (ahpC) and the peroxide regulator operon ahpF-oxyR-orfX from Xanthomonas campestris pv. phaseoli. Journal of Bacteriology. 1997;179(12):3950.
70. Graham JH, Johnson EG, Myers ME, Young M, Rajasekaran P, Das S, et al. Potential of Nano-Formulated Zinc Oxide for Control of Citrus Canker on Grapefruit Trees. Plant Disease. 2016;100(12):2442-7.
71. Hu JH, Wang NA. Evaluation of the Spatiotemporal Dynamics of Oxytetracycline and Its Control Effect Against Citrus Huanglongbing via Trunk Injection. Phytopathology. 2016;106(12):1495-503.
72. Ghosh DK, Kokane S, Kumar P, Ozcan A, Warghane A, Motghare M, et al. Antimicrobial nano-zinc oxide-2S albumin protein formulation significantly inhibits growth of "Candidatus Liberibacter asiaticus" in planta. PLOS ONE. 2018;13(10):e0204702.
73. Philip D, John A, Panicker CY, Varghese HT. FT-Raman, FT-IR and surface enhanced Raman scattering spectra of sodium salicylate. Spectrochimica Acta Part A: Molecular and Biomolecular Spectroscopy. 2001;57(8):1561-6.
74. Volod'Ko L, Huoah L. The vibrational spectra of aqueous nitrate solutions. Journal of Applied Spectroscopy - J APPL SPECTROSC. 1968;9:1100-4.
75. Pettersson M, Tuominen S, Räsänen M. IR Spectroscopic Study of H2O2, HDO2, and D2O2 Isolated in Ar, Kr, and Xe Matrices. The Journal of Physical Chemistry A. 1997;101(6):1166-71.
76. Eysel HH, Thym S. RAMAN Spectra of Peroxides. Zeitschrift für anorganische und allgemeine Chemie. 1975;411(2):97-102.
77. Sirelkhatim A, Mahmud S, Seeni A, Kaus NHM, Ann LC, Bakhori SKM, et al. Review on Zinc Oxide Nanoparticles: Antibacterial Activity and Toxicity Mechanism. Nano-Micro Letters. 2015;7(3):219-42.
78. Etxeberria E, Gonzalez P, Bhattacharya P, Sharma P, Ke PC. Determining the size exclusion for nanoparticles in citrus leaves. HortScience. 2016;51(6):732-7.
79. Lin D, Xing B. Root Uptake and Phytotoxicity of ZnO Nanoparticles. Environmental Science & Technology. 2008;42(15):5580-5.
80. Ruttkay-Nedecky B, Krystofova O, Nejdl L, Adam V. Nanoparticles based on essential metals and their phytotoxicity. Journal of nanobiotechnology. 2017;15(1):33-.
81. Merfa MV, Pérez-López E, Naranjo E, Jain M, Gabriel DW, De La Fuente L. Progress and Obstacles in Culturing 'Candidatus Liberibacter asiaticus', the Bacterium Associated with Huanglongbing. Phytopathology®. 2019;109(7):1092-101.
82. De La Fuente L, Montanes E, Meng Y, Li Y, Burr TJ, Hoch HC, et al. Assessing adhesion forces of type I and type IV pili of Xylella fastidiosa bacteria by use of a microfluidic flow chamber. Appl Environ Microbiol. 2007;73(8):2690-6.
83. Naranjo E, Merfa MV, Santra S, Ozcan A, Johnson E, Cobine PA, et al. Zinkicide Is a ZnO-Based Nanoformulation with Bactericidal Activity against *Liberibacter crescens* in Batch Cultures and in Microfluidic Chambers Simulating Plant Vascular Systems. Appl Environ Microbiol. 2020;86(16):e00788-20.
84. Naranjo E, Merfa MV, Santra S, Ozcan A, Johnson E, Cobine PA, et al. Zinkicide Is a ZnO-Based Nanoformulation with Bactericidal Activity against Liberibacter crescens in Batch Cultures and in Microfluidic Chambers Simulating Plant Vascular Systems. Appl Environ Microbiol. 2020;86(16):e00788-20.
85. Khanal D, Kondyurin A, Hau H, Knowles JC, Levinson O, Ramzan I, et al. Biospectroscopy of nanodiamond-induced alterations in conformation of intra-and extracellular proteins: a nanoscale IR study. Analytical chemistry. 2016;88(15):7530-8.

86. Ruggeri FS, Longo G, Faggiano S, Lipiec E, Pastore A, Dietler G. Infrared nanospectroscopy characterization of oligomeric and fibrillar aggregates during amyloid formation. Nature Communications. 2015;6(1):7831.
87. Zhong J, Liu Y, Ren J, Tang Y, Qi Z, Zhou X, et al. Understanding Secondary Structures of Silk Materials via Micro- and Nano-Infrared Spectroscopies. ACS Biomaterials Science & Engineering. 2019;5(7):3161-83.
88. Ruggeri FS, Mannini B, Schmid R, Vendruscolo M, Knowles TPJ. Single molecule secondary structure determination of proteins through infrared absorption nanospectroscopy. Nature Communications. 2020;11(1):2945.
89. Xiao Y, Liu Y, Zhang W, Qi P, Ren J, Pei Y, et al. Formation, Structure, and Mechanical Performance of Silk Nanofibrils Produced by Heat-Induced Self-Assembly. Macromolecular Rapid Communications.n/a(n/a):2000435.
90. Padmavathy N, Vijayaraghavan R. Enhanced bioactivity of ZnO nanoparticles-an antimicrobial study. Sci Technol Adv Mater. 2008;9(3):035004-.
91. Ortiz de Orué Lucana D, Wedderhoff I, Groves MR. ROS-Mediated Signalling in Bacteria: Zinc-Containing Cys-X-X-Cys Redox Centres and Iron-Based Oxidative Stress. Journal of Signal Transduction. 2012;2012:605905.